A Multi-Domain Approach to the Stabilization of Electrodynamic Levitation Systems

*Original*
A Multi-Domain Approach to the Stabilization of Electrodynamic Levitation Systems / Galluzzi, R., Circosta, S., Amati, N., Tonoli, A., Bonfitto, A., Lembke, T.A., Kertész, M.. - In: JOURNAL OF VIBRATION AND ACOUSTICS. - ISSN 1048-9002. - 142:6(2020). [10.1115/1.4046952]

*Publisher:*
ASME

*Published*
DOI:10.1115/1.4046952

| | |
|---|---|
| Renato | Galluzzi |
| *First* | *Last* |

ASME Paper Title: A Multi-domain Approach to the Stabilization of Electrodynamic Levitation Systems

Authors: Renato Galluzzi, Salvatore Circosta, Nicola Amati, Andrea Tonoli, Angelo Bonfitto, Torbjörn A. Lembke, Milan Kertész

ASME Journal Title: Journal of Vibration and Acoustics

Volume/Issue 142/6 Date of Publication (VOR* Online) May 15, 2020

ASME Digital Collection URL: https://asmedigitalcollection.asme.org/vibrationacoustics/article-abstract/doi/10.1115/1.4046952/1082705/A-Multi-Domain-Approach-to-the-Stabilization-of?redirectedFrom=fulltext

DOI: https://doi.org/10.1115/1.4046952

# A Multi-Domain Approach to the Stabilization of Electrodynamic Levitation Systems

**Renato Galluzzi**[*]
Email: renato.galluzzi@polito.it

**Salvatore Circosta**
Email: salvatore.circosta@polito.it

**Nicola Amati**
Email: nicola.amati@polito.it

**Andrea Tonoli**
Email: andrea.tonoli@polito.it

**Angelo Bonfitto**
Email: angelo.bonfitto@polito.it

Department of Mechanical and Aerospace Engineering
Politecnico di Torino
Corso Duca degli Abruzzi 24 10129 Turin, Italy

**Torbjörn A. Lembke**
Email: torbjorn.lembke@hyperloop.global

**Milan Kertész**
Email: milan.kertesz@hyperloop.global

Hyperloop Transportation Technologies France
135 Avenue du Comminges
31270 Cugnaux, France

---

[*] Corresponding author.

## ABSTRACT

*The Hyperloop transportation system paradigm has gained increasing attention in the last years due to its potential advantages in technology, territory and infrastructure. From an engineering point of view, it would lead to fast, safe, efficient transportation of passengers and cargo. The stability of the electrodynamic levitation system represents a key enabling aspect of Hyperloop. In this context, the state of the art presents numerous attempts to stabilize these systems without definitive guidelines on how to attain proper, stable behavior. Furthermore, research has provided extensive literature in the context of electrodynamic bearings, which requires proper interpretation and generalization into the translational domain. In this paper, we address the stabilization of levitation systems by reproducing the strong interaction between the electrodynamic phenomenon and the mechanical domain. A novel lumped-parameter model with a multiple-branch circuit is proposed and tuned through finite-element simulations to replicate the electrodynamic behavior. The multi-domain equations are linearized and the unstable nature of the levitation system is identified and discussed. Then, a suitable method to add damping and optimize stability is studied. Finally, the linearized model is compared to the nonlinear representation to validate the followed approach.*

*Keywords: Hyperloop, electrodynamic, levitation, stability, eddy currents*

## 1 Introduction

In the last decades, globalization and environmental concerns have driven sensible changes in the mobility paradigm. Transport systems of the future aim at connecting major urban areas by means of increasingly sustainable, fast, safe and efficient technologies. These aspects are nowadays addressed by several government programs worldwide. For example, the Strategic Transport Research and Innovation Agenda (STRIA) of the European Union deals with transport electrification and smart mobility [1].

In this context, the Hyperloop concept has spread as one of these future transportation systems. Based on Robert Goddard's *vactrain* [2], it consists of levitating capsules traveling inside an evacuated tube. Thanks to the low-pressure environment and the levitation technology, the capsule is subject to limited contact with any medium, thus achieving speeds in excess of 1200 km/h. This feature allows the coverage of very large distances in short time and virtually cancels distance gaps between urban areas. Furthermore, the Hyperloop mobility paradigm is ideally zero-emission, since levitation and propulsion systems are fully electrified. Recently, a number of companies has focused in the development and implementation of the Hyperloop concept. The potential of this technology raised the interest of governments that have signed agreements to fund research in this field.

The modern Hyperloop system was proposed in a white paper published by SpaceX in 2013 and released as an open source design [3]. It featured capsules levitated through air bearings, propelled by a linear induction motor and axial compressors, since the use of wheels or any mechanical contact with the track are impractical at very high speed. Then, the idea evolved by replacing air bearings with magnetic pads as in the Inductrack concept [4]. This system relies on the principle of electrodynamic levitation: a capsule equipped with permanent magnets exerts a magnetic field on a conducting track, thus inducing eddy currents that yield lift and drag force components. This levitation architecture enables large air gaps, self-reliability, low component count and simplicity. Furthermore, it is fully passive and no cryogenic cooling systems are needed as in the superconducting electrodynamic levitation [5]. The lift-to-drag ratio increases with speed, thus making the Inductrack technology very appealing for very high speed applications. In this scenario, the Hyperloop concept becomes an interesting, more efficient alternative to traditional transportation systems.

The levitation subsystem represents a key enabling technology in Hyperloop. In particular, there is interest in implementing stable, passive levitation through electrodynamic means. In this context, scientific research in the field of electrodynamic bearings (EDB) for rotating machines is a point of reference. Tonoli *et al.* [6–9], Filatov *et al.* [10] and Lembke [11–14] have studied different configurations of EDBs through modeling and experiments, identified their unstable nature and stabilized them through diverse techniques. In recent efforts, Van Verdeghem *et al.* have investigated rotating systems equipped with thrust EDBs [15]. They also determined numerically the minimum amount of damping required for stabilization [16].

Being a translational variant of the EDBs, passive levitation of moving pods require stabilization. Post *et al.* [4, 17] first described this behavior in the frame of the Inductrack project, while giving less emphasis on the methods to tackle instability. Specifically, the Inductrack vehicle had a relatively short track for its size and therefore, stability issues were hardly observable during the tests [18].

In 2002, General Atomics rekindled the concept of passive magnetic levitation transportation [19, 20]. They managed to develop a full-scale prototype able to operate safely during levitation. However, in many cases, the prototype reached a larger-than-expected air gap, which was bounded by auxiliary wheels. This safety mechanism could easily have masked the unstable nature of the system.

In more recent efforts, Storset *et al.* have indicated that electrodynamic levitation systems present an intrinsic low-damping behavior that requires additional damping sources to ensure stable operation [21]. Likewise, other research groups have followed this concept in a heuristic fashion [22, 23]. Although the attained results are valid in some cases, this approach fails to capture the essence of electrodynamic levitation instability.

General Atomics also built a test setup to reproduce the force behavior in levitation using a rotating conductive drum and a permanent-magnet array. This rig layout has been replicated and studied by numerous research groups with the same objective [24–26]. In many of these experiences, particular difficulty is found when reproducing the force behavior through analytical models, as heavy nonlinear contributions are found at high speed.

Recently, student teams participating in the SpaceX Hyperloop Pod Competition have also dealt with the aforementioned aspects regarding the stabilization and experimental characterization of electrodynamic levitation systems [27, 28].

This scenario demonstrates that, although passive levitation transport systems have gained a substantial technological momentum in the last decade, aspects regarding their stabilization remain partially unexplored. As already stated, some works in the field of EDBs have addressed stability both from theoretical and experimental perspectives. Nevertheless, their extension to systems of translational nature over solid conductor tracks requires important considerations.

The present research establishes an integrated model with the aim of reproducing the intrinsic instability in levitation systems. The proposed approach is general and systematic; by following it, the designer can reproduce the unstable behavior on any degree of freedom. Moreover, it allows linearization and hence, the use of root locus tools. To reach this objective, the method exploits a multiple-branch circuit in the electrical domain that recreates accurately the electrodynamic phenomenon.

The unstable nature in magnetic levitation systems rises from the strong interaction between the electrodynamic phenomenon and the mechanical domain. However, the instability takes place in the mechanical degrees of freedom. This intrinsic coupling can be taken into account only through a multi-domain approach, which subsequently allows defining of a method to stabilize the system.

The remainder of this work is organized as follows. Section 2 focuses on the electrodynamic levitation modeling. It discusses both finite-element and lumped-parameter formulations of the problem. On this base, the lumped parameters of the levitation system are fitted from the finite-element problem solution. Section 3 deals with the integration between electromagnetic and mechanical domain equations. Stability aspects are studied for the levitation system with one and two degrees of freedom. In Sec. 4, simulations are performed in time and frequency domains to compare the behavior of the linear and nonlinear versions of the model developed in Sec. 3. Finally, Sec. 5 concludes the work.

## 2 Levitation System

For demonstration purposes, the present study refers to the two-dimensional geometry shown in Fig. 1 and its parameters listed in Table 1. The pad consists of a Halbach array of NdFeB permanent magnets (PM), as proposed by Post [18]. The track, by converse, is an aluminum slab that follows the specifications provided by SpaceX for the Hyperloop Pod Competition [29].

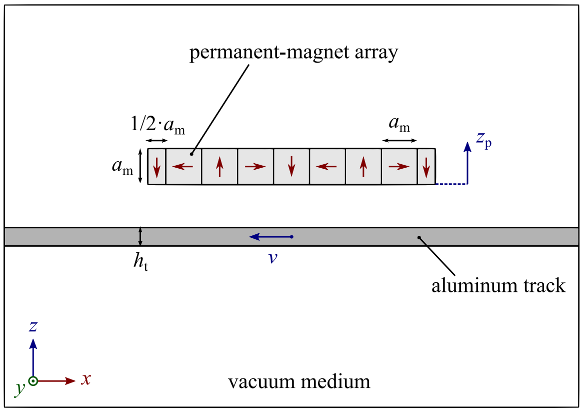

Fig. 1: Two-dimensional geometry of the levitation system. Refer to Table 1 for parameters and dimensions.

Table 1: Dimensions and parameters of the levitation system.

| Domain | Feature | Symbol | Value | Unit |
|---|---|---|---|---|
| N45UH NdFeB PM array | Number of pole pairs | $N_\mathrm{p}$ | 2 | – |
| | Number of magnets per pole pair | $N_\mathrm{m}$ | 4 | – |
| | Magnet side length | $a_\mathrm{m}$ | 25 | mm |
| | Magnet in-plane depth | $d_\mathrm{m}$ | 125 | mm |
| | Remanent magnetic flux density* | $B_\mathrm{r}$ | 1.29 | T |
| | Resistivity* | $\rho_\mathrm{m}$ | 181.44 | $\mu\Omega\cdot$cm |
| | Relative magnetic permeability | $\mu_{\mathrm{r,m}}$ | 1.06 | – |
| 6101-T61 aluminum | Thickness | $h_\mathrm{t}$ | 12.7 | mm |
| | Resistivity* | $\rho_\mathrm{t}$ | 3.51 | $\mu\Omega\cdot$cm |
| | Relative magnetic permeability | $\mu_{\mathrm{r,t}}$ | 1 | – |

* at a temperature of 60°C

### 2.1 Finite-element model

The geometry in Fig. 1 can be used to build a finite-element (FE) model that reproduces the behavior of the levitation system. Aluminum and PM domains are represented by their electrical conductivity $\sigma = 1/\rho$ and relative magnetic permeability $\mu_\mathrm{r}$, whereas the vacuum medium in which the system works has $\sigma_\mathrm{v} = 0$ and $\mu_{\mathrm{r,v}} = 1$.

For each domain, the following problem formulation is established to solve for the magnetic vector potential **A**:

$$\mathbf{B} = \nabla \times \mathbf{A} \tag{1}$$

$$\nabla \times \mathbf{H} = \mathbf{J} \tag{2}$$

where **B** is the magnetic flux density, **H** is the magnetic field and **J** is the current density.

Furthermore, each domain obeys the Ampère's law through the constitutive relation

$$\mathbf{B} = \mu_0 \mu_\mathrm{r} \mathbf{H} \tag{3}$$

where $\mu_0 = 4\pi \cdot 10^{-7}$ H/m is the magnetic permeability of the vacuum. In the case of the permanent magnets, Eq. (3) is modified by adding the remanence vector $\mathbf{B}_\mathrm{r}$, which is set for each magnet according to the direction of magnetization.

The aluminum track is set to move in horizontal direction through a constant velocity vector $\mathbf{v}$. The electrodynamic interaction is reproduced by applying a Lorentz term to compute the current density distribution inside the track:

$$\mathbf{J} = \sigma (\mathbf{v} \times \mathbf{B}) \tag{4}$$

The proposed geometry presents a sufficiently large in-plane depth to allow neglecting the end effect of the eddy currents:

$$d_\mathrm{m} > N_\mathrm{m} a_\mathrm{m} / 2 \tag{5}$$

and hence, a two-dimensional representation is possible.

In practice, the described model was implemented in COMSOL Multiphysics. Domains were meshed using a triangular distribution for an approximate total of 24 thousand elements. For accurate eddy current reproduction, the maximum element size inside the aluminum track was set to 2 mm. Force components were assessed by applying the Maxwell stress tensor to the PM array. Referring to the Cartesian reference frame in Fig. 1, the lift force component is vertical (positive along $z$), while the drag force component is horizontal (positive along $-x$).

For verification purposes, Fig. 2 presents simulation results obtained at a constant, uniform air gap of 5 mm and longitudinal velocities of 1 and 340 m/s. The contours in Fig. 2 represent the out-of-plane component of $\mathbf{A}$ and give an idea of the flux distribution, whereas the color maps depict the out-of-plane current density distribution inside the track. In qualitative terms, the model captures successfully the behavior of the levitation system. At 1 m/s, eddy currents form loops that follow the magnet pole distribution of the PM array. These currents cover

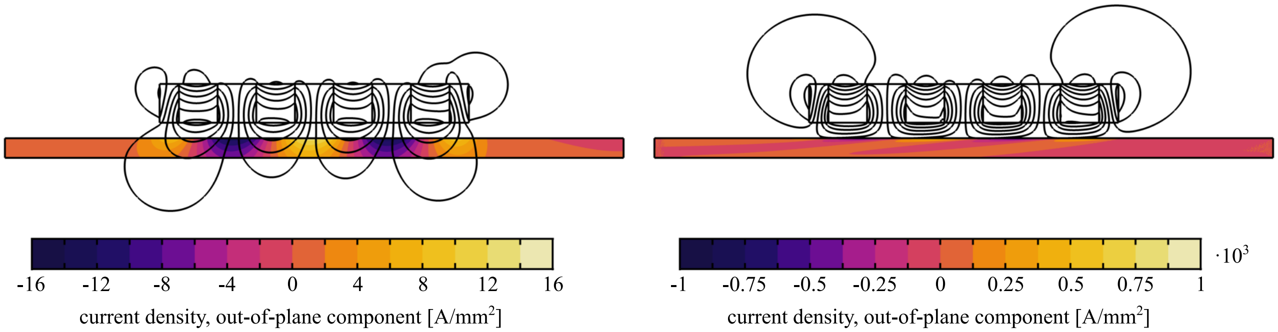

(a) $v = 1\ \mathrm{m/s}$ (b) $v = 340\ \mathrm{m/s}$

Fig. 2: FE model results with an air gap of $5\ \mathrm{mm}$ and longitudinal speed values of $1\ \mathrm{m/s}$ and $340\ \mathrm{m/s}$. The out-of-plane components of the current density (color map) and the magnetic vector potential (contours) are displayed.

the entire track, although they appear with stronger intensity towards its top surface due to the vicinity of the magnets. Also, flux lines enclose the track without any obstruction. By converse, at 340 m/s, the magnitude of the current density increases drastically, but it concentrates predominantly on the top of the track, thus exhibiting the well-known skin effect. As a consequence, a shielding phenomenon takes place, where the flux lines find an obstacle and do not pass through the track.

It is worth stressing out that these simulations are stationary, as they do not account for the dynamic interaction between the developed force components and the elements in the mechanical domain. However, they prove usefulness by computing the electromagnetic characteristics of the levitation system. The obtained results enable the tuning of a lumped-parameter model representation that can be subsequently coupled with the mechanical domain, as already proven for EDBs [6–9].

### 2.2 Lumped-parameter model

The electrodynamic levitation phenomenon presents an intrinsic nonlinear nature, as observed from the FE model results. Moreover, it features a strong interaction between the electromagnetic and mechanical domains. To facilitate the analysis, we propose the use of a lumped-parameter model that can be easily coupled with the mechanical domain. Similar approaches have been followed for EDB systems in the past [6–9].

The followed method does not lose generality because models are expressed in terms of physical quantities found in any system featuring electrodynamic levitation.

Although the levitation system works over a continuous aluminum track, the distribution of the flux and current density vectors in space allow for a lumped coil representation. This goes well in agreement with the approaches followed for EDB systems [7] and solid rotor induction machines [30].

Starting on a reference frame fixed to the track, one can express in complex notation the permanent magnet

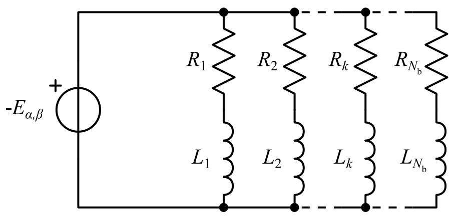

Fig. 3: Equivalent circuit of the current path inside the track conductor with multiple branches in electrical parallel. For simplicity, the circuit is represented for a generic BEMF component $\alpha,\beta$. Each branch is characterized by specific resistance and inductance values.

flux linkage $\lambda$ acting on two orthogonal coils within the track continuum:

$$\lambda = \Lambda \mathrm{e}^{\mathrm{j}\omega t} \tag{6}$$

where the periodicity of excitation is denoted by the pole pitch ratio $\gamma$:

$$\omega = v/\gamma \tag{7}$$

$$\gamma = \frac{N_\mathrm{m} a_\mathrm{m}}{2\pi} \tag{8}$$

The amplitude of the excitation ($\Lambda$) is an exponential function of the air gap [4] according to

$$\Lambda = \Lambda_0 \mathrm{e}^{-\frac{z_\mathrm{p}}{\gamma}} \tag{9}$$

Thus, the back-electromotive force (BEMF) on the track is given by

$$E = \frac{\mathrm{d}\lambda}{\mathrm{d}t} = E_\alpha + \mathrm{j}E_\beta = \frac{\partial \Lambda}{\partial z_\mathrm{p}} \dot{z}_\mathrm{p} \mathrm{e}^{\mathrm{j}\omega t} + \mathrm{j}\omega\Lambda \mathrm{e}^{\mathrm{j}\omega t} \tag{10}$$

where subindexes $\alpha$ and $\beta$ denote orthogonal axes relative to a fixed reference frame.

In this approach, we propose to represent the dynamic behavior of the current path inside the track conductor as the electrical parallel of $N_\mathrm{b}$ branches characterized by specific resistance and inductance values, as observed in Fig. 3.

For the $k$th branch, the circuit equation is written as

$$L_k \frac{\mathrm{d}i_k}{\mathrm{d}t} + R_k i_k + E = 0 \tag{11}$$

being $L_k$ and $R_k$ the characteristic inductance and resistance of the $k$th branch and $i_k$ the current flowing through it.

Substituting Eq. (10) into Eq. (11) and expressing the circuit in a moving (rotating) frame through $i_k = i_{\mathrm{r},k}\mathrm{e}^{\mathrm{j}\omega t}$ yields

$$L_k \frac{\mathrm{d}i_{\mathrm{r},k}}{\mathrm{d}t} + R_k i_{\mathrm{r},k} + \mathrm{j}\omega L_k i_{\mathrm{r},k} + \frac{\partial \Lambda}{\partial z_{\mathrm{p}}}\dot{z}_{\mathrm{p}} + \mathrm{j}\omega\Lambda = 0 \tag{12}$$

For ease of notation, Eq. (12) can be expressed in terms of direct (d) and quadrature (q) axis components, since $i_{\mathrm{r},k} = i_{\mathrm{d},k} + \mathrm{j}i_{\mathrm{q},k}$. In addition, the impedance of the $k$th branch can be described through its electromagnetic pole frequency $\omega_{\mathrm{p},k} = R_k/L_k$, hence

$$\frac{\mathrm{d}i_{\mathrm{d},k}}{\mathrm{d}t} = -\omega_{\mathrm{p},k} i_{\mathrm{d},k} + \omega i_{\mathrm{q},k} - \frac{E_{\mathrm{d}}}{L_k} \tag{13}$$

$$\frac{\mathrm{d}i_{\mathrm{q},k}}{\mathrm{d}t} = -\omega_{\mathrm{p},k} i_{\mathrm{q},k} - \omega i_{\mathrm{d},k} - \frac{E_{\mathrm{q}}}{L_k} \tag{14}$$

where

$$E_{\mathrm{d}} = \frac{\partial \Lambda}{\partial z_{\mathrm{p}}}\dot{z}_{\mathrm{p}} \tag{15}$$

$$E_{\mathrm{q}} = \Lambda\omega \tag{16}$$

To calculate the power balance of the system for the $k$th branch, we first multiply Eq. (13) by $i_{\mathrm{d},k}$ and Eq. (14)

by $i_{\mathrm{q},k}$. Then, both contributions are added:

$$\underbrace{L_k i_{\mathrm{d},k}\frac{\mathrm{d}i_{\mathrm{d},k}}{\mathrm{d}t}+L_k i_{\mathrm{q},k}\frac{\mathrm{d}i_{\mathrm{q},k}}{\mathrm{d}t}}_{1^{\mathrm{st}}\text{ pair}}+\underbrace{R_k i_{\mathrm{d},k}^2+R_k i_{\mathrm{q},k}^2}_{2^{\mathrm{nd}}\text{ pair}}+\underbrace{E_\mathrm{d} i_{\mathrm{d},k}+E_\mathrm{q} i_{\mathrm{q},k}}_{3^{\mathrm{rd}}\text{ pair}}=0 \tag{17}$$

The first pair of terms from Eq. (17) denotes the rate of change of stored magnetic energy. The second pair indicates the dissipated power by Joule effect. The last pair belongs to the mechanical power developed by the levitation system, from which lift and drag forces can be computed. Assuming the superposition of $N_\mathrm{b}$ circuit branches, these force components are given by

$$F_\mathrm{lift}=\frac{E_\mathrm{d}}{\dot{z}_\mathrm{p}}\sum_{k=1}^{N_\mathrm{b}} i_{\mathrm{d},k}=\frac{\partial\Lambda}{\partial z_\mathrm{p}}\sum_{k=1}^{N_\mathrm{b}} i_{\mathrm{d},k} \tag{18}$$

$$F_\mathrm{drag}=-\frac{E_\mathrm{q}}{v}\sum_{k=1}^{N_\mathrm{b}} i_{\mathrm{q},k}=-\frac{\Lambda}{\gamma}\sum_{k=1}^{N_\mathrm{b}} i_{\mathrm{q},k} \tag{19}$$

In static conditions—constant vertical pad position $z_\mathrm{p}$ and constant longitudinal speed $v$—the derivative terms in Eqs. (13) and (14) vanish. Therefore, one can solve for direct and quadrature axis currents and compute analytically the behavior of $F_\mathrm{lift}$ and $F_\mathrm{drag}$ as

$$F_\mathrm{lift}=\frac{\Lambda_0^2}{\gamma}\mathrm{e}^{-\frac{2z_\mathrm{p}}{\gamma}}\sum_{k=1}^{N_\mathrm{b}}\frac{\omega^2/\omega_{\mathrm{p},k}^2}{L_k\left(1+\omega^2/\omega_{\mathrm{p},k}^2\right)} \tag{20}$$

$$F_\mathrm{drag}=\frac{\Lambda_0^2}{\gamma}\mathrm{e}^{-\frac{2z_\mathrm{p}}{\gamma}}\sum_{k=1}^{N_\mathrm{b}}\frac{\omega/\omega_{\mathrm{p},k}}{L_k\left(1+\omega^2/\omega_{\mathrm{p},k}^2\right)} \tag{21}$$

Equations (20) and (21) can be also written in the mechanical domain by means of the electromagnetic stiff-

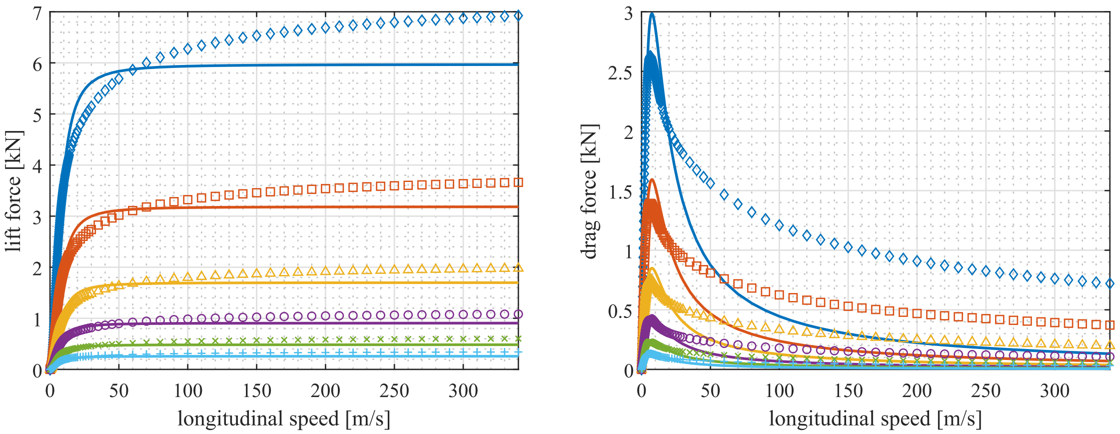

(a) Model fit with one circuit branch

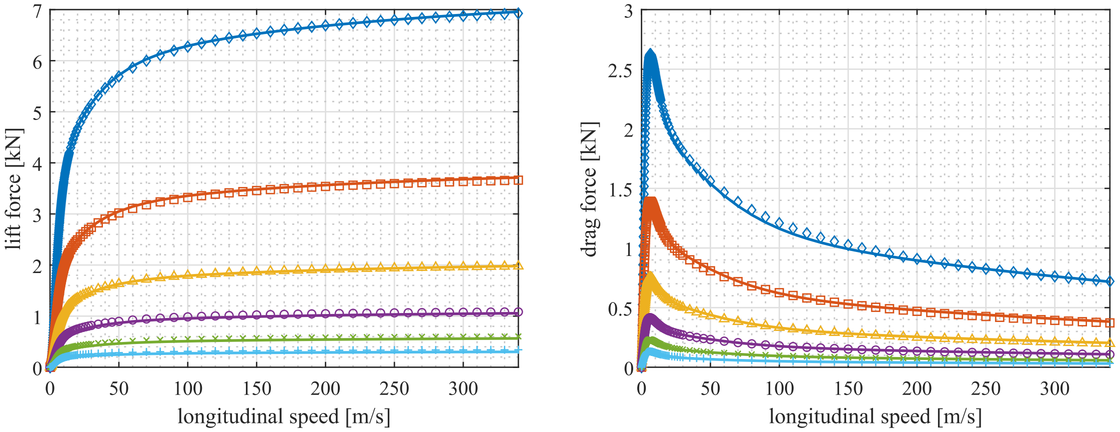

(b) Model fit with three circuit branches

Fig. 4: Lift and drag force components of the levitation system. FE model results were obtained for constant longitudinal velocities ranging from $0$ to $340\,\mathrm{m/s}$ and air gap values of $5\,\mathrm{mm}$ (diamond), $10\,\mathrm{mm}$ (square), $15\,\mathrm{mm}$ (triangle), $20\,\mathrm{mm}$ (circle), $25\,\mathrm{mm}$ (cross) and $30\,\mathrm{mm}$ (plus sign). These data were fitted with the proposed model (solid) using one and three electrical circuit branches.

ness $k_{\mathrm{e},k}$ and damping $c_{\mathrm{e},k}$, where

$$k_{\mathrm{e},k} = \frac{\Lambda_0^2}{L_k} \tag{22}$$

$$c_{\mathrm{e},k} = \frac{\Lambda_0^2}{R_k} \tag{23}$$

$$\omega_{\mathrm{p},k} = \frac{k_{\mathrm{e},k}}{c_{\mathrm{e},k}} \tag{24}$$

Static lift and drag can be easily reproduced with the aid of the FE model of Sec. 2.1. To this end, the model was simulated for longitudinal velocities ranging from 0 to 340 m/s (165 values) and air gap values from 5 to 30 mm (6 values) for a total of 990 parameter combinations. The obtained results were fitted with the static force analytical Eqs. (20) and (21), where the objective was to find suitable values for pole frequency terms $\omega_{\mathrm{p},k}$ and

Table 2: Output of the lumped-parameter model fitting with FE model data.

| Feature | Unit | $N_\mathrm{b} = 1$ | $N_\mathrm{b} = 2$ | $N_\mathrm{b} = 3$ | $N_\mathrm{b} = 4$ |
|---|---|---|---|---|---|
| Fit error | kN | 8.13 | 1.44 | 0.84 | 0.82 |
| Branch pole frequency | rad/s | $\omega_{\mathrm{p},1} = 471.59$ | $\omega_{\mathrm{p},1} = 372.98$<br>$\omega_{\mathrm{p},2} = 4.51 \cdot 10^3$ | $\omega_{\mathrm{p},1} = 355.45$<br>$\omega_{\mathrm{p},2} = 2.57 \cdot 10^3$<br>$\omega_{\mathrm{p},3} = 1.73 \cdot 10^4$ | $\omega_{\mathrm{p},1} = 353.32$<br>$\omega_{\mathrm{p},2} = 2.31 \cdot 10^3$<br>$\omega_{\mathrm{p},3} = 1.01 \cdot 10^4$<br>$\omega_{\mathrm{p},4} = 2.06 \cdot 10^{10}$ |
| Branch inductance* | H | $L_1 = 6.07 \cdot 10^{-10}$ | $L_1 = 7.35 \cdot 10^{-10}$<br>$L_2 = 1.74 \cdot 10^{-9}$ | $L_1 = 7.72 \cdot 10^{-10}$<br>$L_2 = 2.06 \cdot 10^{-9}$<br>$L_3 = 4.12 \cdot 10^{-9}$ | $L_1 = 7.77 \cdot 10^{-10}$<br>$L_2 = 2.26 \cdot 10^{-9}$<br>$L_3 = 4.49 \cdot 10^{-9}$<br>$L_4 = 2.34 \cdot 10^{-14}$ |

* after determining $\Lambda_0 = 0.33$ mWb

electromagnetic stiffness terms $k_{\mathrm{e},k}$.

This process was repeated for models with different number of branches $N_\mathrm{b}$. The fitting was performed by minimizing the $l^2$-norm of the force error through an interior-point algorithm for constrained optimization in MATLAB.

Figure 4 compares the force outputs of the FE model and the lumped-parameter model fit with one and three circuit branches. With a single branch, the lumped-parameter model cannot reproduce the behavior of the levitation system inside the whole speed range, mainly because the skin effect becomes predominant at increasing speed. This aspect is particularly evident when using a solid, continuous track for levitation. By adding more *RL* elements, each branch is tuned to satisfy a specific portion of the speed range. In particular, the model with three branches captures successfully the behavior of the levitation system up to 340 m/s.

Moreover, we list the fitting results for models with one to four branches in Table 2. Note that the fit error difference between three and four branches is negligible, thus confirming that $N_\mathrm{b} = 3$ is a suitable choice.

Finally, a numeric value of the flux linkage term $\Lambda_0$ could be useful to determine the inductance $L_k$ using Eq. (22). Accordingly, a FE computation at null longitudinal speed and constant gap can be performed. The aluminum track is sectioned into coil paths where eddy currents usually take place. Then, the flux linkage is computed from the well-known expression [31]

$$\Lambda = \frac{L}{S}\left(\int_{S+} A_y \mathrm{d}S - \int_{S-} A_y \mathrm{d}S\right) \tag{25}$$

where $A_y$ is the out-of-plane component of the magnetic vector potential and $S$ is the coil cross section. The signs denote the paths where the current density goes inward ($-$) or outward the plane ($+$). Afterwards, $\Lambda_0$ can be obtained from $\Lambda$ by using Eq. (9).

## 3 Vertical Dynamics

### 3.1 Single-degree-of-freedom stability

In the mechanical domain, it is possible to study the stability of the levitation system constituted by a PM pad rigidly attached to a cart. Assuming a moving mass to levitate $m_\mathrm{t} = 22$ kg [18], vertical dynamics can be analyzed through

$$\ddot{z}_\mathrm{p} = \frac{F_\mathrm{lift}}{m_\mathrm{t}} - \mathrm{g} \tag{26}$$

where $\mathrm{g} = 9.81\ \mathrm{m/s^2}$ is the gravity acceleration. The force term $F_\mathrm{lift}$ recalls Eq. (18), which in turn lumps the d axis current contribution from each circuit branch. These current components are obtained by solving the differential equation set constituted by Eqs. (13) and (14).

To analyze stability, the aforementioned model is linearized, specifically Eqs. (13), (14) and (18). With a linear representation of the system, such as the state-space form, the poles of the system can be computed to evaluate stability. The root locus is a useful graphical tool to perform this assessment.

From Eq. (9), a linearized flux linkage amplitude can be expressed around a vertical displacement $z_{\mathrm{p},0}$:

$$\bar{\Lambda} = \Lambda_0 \mathrm{e}^{-\frac{z_{\mathrm{p},0}}{\gamma}} - \frac{\Lambda_0}{\gamma}\mathrm{e}^{-\frac{z_{\mathrm{p},0}}{\gamma}}\left(z_\mathrm{p} - z_{\mathrm{p},0}\right) \tag{27}$$

and hence, the electrical circuit equations of the $k$th branch are rewritten as follows

$$\frac{\mathrm{d}i_{\mathrm{d},k}}{\mathrm{d}t} = -\omega_{\mathrm{p},k} i_{\mathrm{d},k} + \omega i_{\mathrm{q},k} + \frac{\Lambda_0}{\gamma L_k}\mathrm{e}^{-\frac{z_{\mathrm{p},0}}{\gamma}}\dot{z}_\mathrm{p} \tag{28}$$

$$\frac{\mathrm{d}i_{\mathrm{q},k}}{\mathrm{d}t} = -\omega_{\mathrm{p},k} i_{\mathrm{q},k} - \omega i_{\mathrm{d},k} + \frac{\omega\Lambda_0}{\gamma L_k}\mathrm{e}^{-\frac{z_{\mathrm{p},0}}{\gamma}}\left(z_\mathrm{p} - z_{\mathrm{p},0}\right) - \frac{\omega\Lambda_0}{L_k}\mathrm{e}^{-\frac{z_{\mathrm{p},0}}{\gamma}} \tag{29}$$

and the lift force expression in Eq. (18) is linearized as

$$\bar{F}_{\text{lift}} = -\sum_{k=1}^{N_{\text{b}}} \left( \frac{\Lambda_0^2}{\gamma L_k} \mathrm{e}^{-\frac{2z_{\text{p},0}}{\gamma}} + \frac{2\Lambda_0}{\gamma} \mathrm{e}^{-\frac{z_{\text{p},0}}{\gamma}} i_{\text{d},k} \right) \tag{30}$$

Equations (26) and (28) to (30) are arranged into the state matrix $\mathbf{A}_1$, as presented in Appendix A. Subsequently, poles are calculated and plotted in the complex plane. Note that the linear nature of this representation requires constant longitudinal speed $v = \gamma\omega$. Therefore, the computation of these poles at different values of $v$ yields a locus that depicts the evolution of the system stability at increasing longitudinal speed.

Since the vertical position of the PM pad is fixed through the linearization point $z_{\text{p},0}$, several root loci can be obtained at different air gap values. However, this situation does not depict the normal operation of the levitation system. Given that electrodynamic levitation must counteract the weight of the system, the pad experiences an imposed constant load. Consequently, the air gap adapts to guarantee static equilibrium between the weight and the lift force.

A simple way to impose the weight load to the system is to calculate the value of $z_{\text{p},0}$ that satisfies this constraint within the speed range of interest. In static condition, Eq. (20) matches the weight force $m_{\text{t}}g$ and the levitation air gap is obtained as

$$z_{\text{p},0}(\omega) = -\frac{\gamma}{2} \ln \left( \frac{m_{\text{t}} g \gamma}{\Lambda_0^2 \Gamma(\omega)} \right) \tag{31}$$

where the auxiliary term $\Gamma(\omega)$ has been introduced:

$$\Gamma(\omega) = \sum_{k=1}^{N_{\text{b}}} \frac{\omega^2/\omega_{\text{p},k}^2}{L_k \left( 1 + \omega^2/\omega_{\text{p},k}^2 \right)} \tag{32}$$

At speed below 0.89 m/s, the lift force is not sufficient to contrast the weight of the cart. Figure 5 illustrates the behavior of $z_{\text{p},0}$ at longitudinal speed values ranging from 0.89 to 340 m/s. By following this air gap profile, it is possible to extract the root locus of the levitation system for different speeds and imposed load. This result is found in Fig. 6, where the poles are plotted at increasing speed, as denoted by the arrows.

The complete locus in Fig. 6 shows the dynamic behavior of three electrical branches. Each pole set is

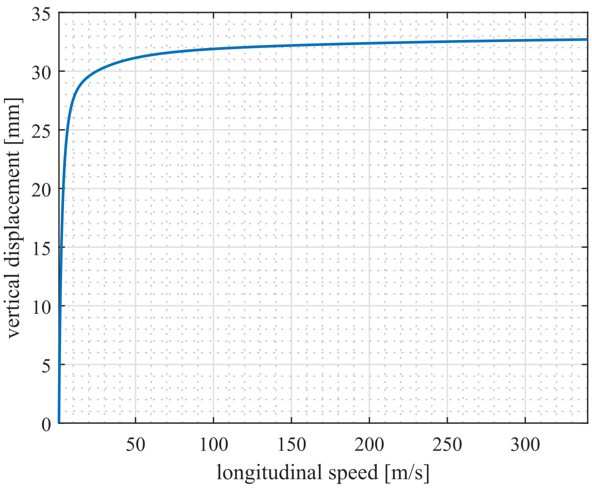

Fig. 5: Behavior of the vertical displacement of the pad as a function of the longitudinal speed ranging from $0$ to $340\ \mathrm{m/s}$. The low-speed points at which levitation is not possible have been omitted.

complex conjugate due to the interaction between $i_{\mathrm{d},k}$ and $i_{\mathrm{q},k}$; its real value converges asymptotically to the electromagnetic pole frequency $-\omega_{\mathrm{p},k}$ as speed increases. Hence, the poles related to the electromagnetic domain are always stable.

A closer insight nearby the origin of the complex plain highlights two mechanical poles. At 0.89 m/s, they assume real, stable values of $s = -9.18$ rad/s and $s = -317.9$ rad/s. Then, the poles merge along the real axis into $s = -38.61$ rad/s at a speed of 1.28 m/s. Subsequently, they break away as complex poles tending to instability. The imaginary axis crossover occurs at a speed of 6.4 m/s, where both poles have a natural frequency of 35.04 rad/s. After this point, mechanical poles lie always in the right side of the complex plane. Therefore, the levitation system is unstable beyond 6.4 m/s, which constitutes almost the entirety of the longitudinal speed range.

In literature, the levitation system is usually modeled using an equivalent stiffness representation [22, 23]. This parameter can be calculated as

$$k_{\mathrm{p}} = -\frac{\partial F_{\mathrm{lift}}}{\partial z_{\mathrm{p}}} = \frac{2\Lambda_0^2}{\gamma^2} \mathrm{e}^{-\frac{2z_{\mathrm{p}}}{\gamma}} \Gamma(\omega) \tag{33}$$

To reproduce the imposed load condition, Eq. (31) is substituted into Eq. (33) and the equivalent stiffness becomes

$$k_{\mathrm{p}} = \frac{2m_{\mathrm{t}}\mathrm{g}}{\gamma} = 27.12\ \mathrm{kN/m} \tag{34}$$

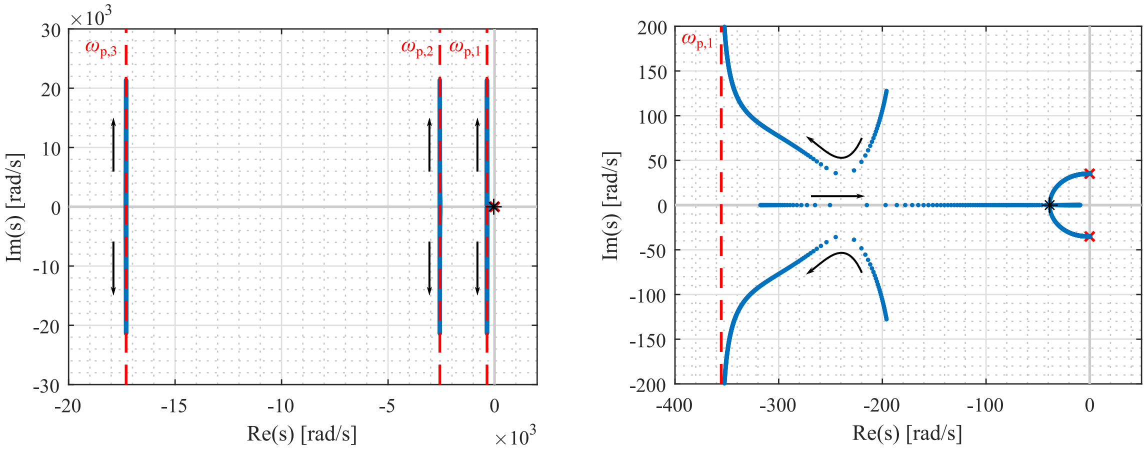

(a) Complete locus

(b) Zoom-in: mechanical and first branch poles

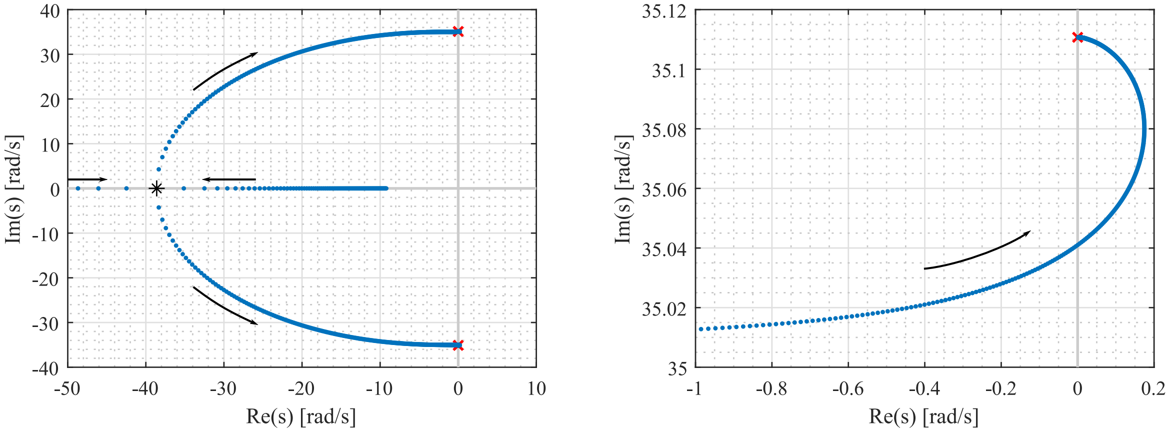

(c) Zoom-in: mechanical poles

(d) Zoom-in: instability

Fig. 6: Root locus of the single-degree-of-freedom system (dot) at increasing longitudinal speed (arrows). The electromagnetic pole frequencies are marked as asymptotes (dashed). The point where the mechanical poles merge is highlighted (asterisk). The poles of the system when the pad is modeled as an equivalent stiffness are also indicated (cross).

which is independent of the vertical displacement or longitudinal speed. The poles of a mass-spring system are imaginary and, as demonstrated by Post and Ryutov [4], their natural frequency is independent of the cart mass:

$$\omega_\mathrm{n} = \sqrt{\frac{k_\mathrm{p}}{m_\mathrm{t}}} = \sqrt{\frac{2\mathrm{g}}{\gamma}} = 35.11\ \mathrm{rad/s} \tag{35}$$

In Fig. 6, we also depict these imaginary poles. It is observed that the behavior of the poles obtained with the proposed approach tend to $\pm \mathrm{j}\omega_\mathrm{n}$ as $v \to \infty$. Nevertheless, the equivalent-stiffness formulation used in literature states that the system is marginally stable at worst. Unlike the approach presented in this paper, it fails in reproducing the evolution of instability of the levitation system.

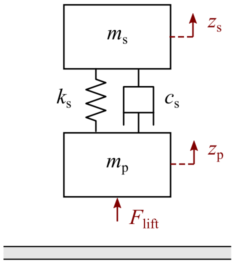

Fig. 7: Quarter-car model of the levitation system.

### 3.2 Two-degree-of-freedom stability

To stabilize the single-degree-of-freedom configuration, damping must be introduced into the system. A possible solution is to install a suspension between the PM pad and the cart. In this way, the system assumes the well-known layout of a quarter-car model, as depicted in Fig. 7. The moving mass is split into $m_\mathrm{t} = m_\mathrm{s} + m_\mathrm{p}$, being $m_\mathrm{s} = 20$ kg the sprung mass and $m_\mathrm{p} = 2$ kg the unsprung mass. The two bodies are connected by means of a suspension constituted by spring $k_\mathrm{s}$ and viscous damper $c_\mathrm{s}$ in parallel.

The mechanical domain equations of this configuration are given by

$$\ddot{z}_\mathrm{p} = \frac{F_\mathrm{lift}}{m_\mathrm{p}} + \frac{c_\mathrm{s}}{m_\mathrm{p}}\left(\dot{z}_\mathrm{s} - \dot{z}_\mathrm{p}\right) + \frac{k_\mathrm{s}}{m_\mathrm{p}}\left(z_\mathrm{s} - z_\mathrm{p}\right) - \mathrm{g} \tag{36}$$

$$\ddot{z}_\mathrm{s} = -\frac{c_\mathrm{s}}{m_\mathrm{s}}\left(\dot{z}_\mathrm{s} - \dot{z}_\mathrm{p}\right) - \frac{k_\mathrm{s}}{m_\mathrm{s}}\left(z_\mathrm{s} - z_\mathrm{p}\right) - \mathrm{g} \tag{37}$$

The suspension stiffness $k_\mathrm{s}$ can be tuned to lead to a natural frequency of the sprung mass $\omega_\mathrm{n,s} = 6.28\ \mathrm{rad/s}$. The traditional approach in automotive systems considers the degrees of freedom uncoupled. This assumption holds if the natural frequencies of both masses are at least one decade apart. Hence, the suspension stiffness can be approximated as

$$k_\mathrm{s} \cong m_\mathrm{s}\omega_\mathrm{n,s}^2 = 789.57\ \mathrm{N/m} \tag{38}$$

Equations (28) to (30), (36) and (37) can be arranged into the state matrix $\mathbf{A}_2$, as presented in Appendix A, to compute and plot the system poles in a root locus. Equation (31) is also necessary to reproduce the behavior at imposed load.

Without damping, the quarter-car system exhibits the behavior in Fig. 8. In the electromagnetic domain, the results are very similar to those shown in Sec. 3.1: stable asymptotic behavior at $\omega_{\mathrm{p},k} \forall k = 1,2,3$. For the unsprung

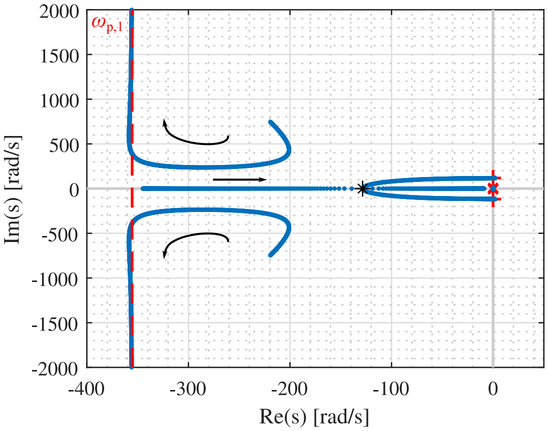

(a) Zoom-in: mechanical and first branch poles

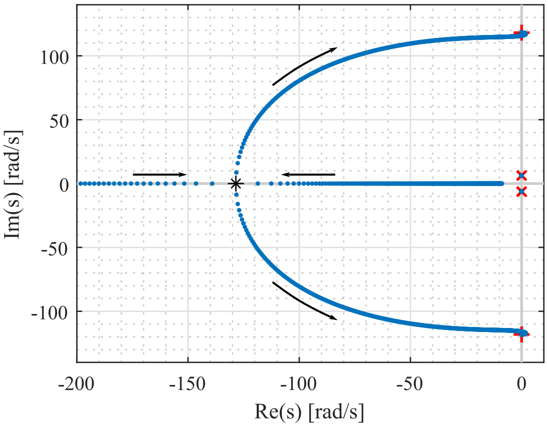

(b) Zoom-in: mechanical poles

Fig. 8: Root locus of the two-degree-of-freedom system (dot) at increasing longitudinal speed (arrows), without suspension damping. The electromagnetic pole frequency of the first branch is marked as an asymptote (dashed). The point where the unsprung mass poles merge is highlighted (asterisk). The poles of the sprung mass are imaginary and do not change with speed (cross). The poles of the unsprung mass when the pad is modeled as an equivalent stiffness are also indicated (plus sign).

mass degree of freedom, the system presents stable, real poles at take-off (0.89 m/s) with $s = -8.82$ rad/s and $s = -344.9$ rad/s. Pole merging occurs at 2.19 m/s ($s = -128.5$ rad/s). Instability is reached beyond 6.69 m/s. As for the single degree of freedom, the system is unstable for a predominant operating range, but it tends to marginal stability as $v \to \infty$. In an equivalent-stiffness representation, the natural frequency of this degree of freedom could be approximated as

$$\omega_{\mathrm{n,p}} \cong \sqrt{\frac{k_{\mathrm{p}} + k_{\mathrm{s}}}{m_{\mathrm{p}}}} = 118.13\ \mathrm{rad/s} \tag{39}$$

In contrast, the sprung mass yields two imaginary poles at $\pm j\omega_{\mathrm{n,s}}$ that do not shift with the longitudinal speed. The obtained values for $\omega_{\mathrm{n,p}}$ and $\omega_{\mathrm{n,s}}$ justify the initial assumption of uncoupled dynamics among the degrees of

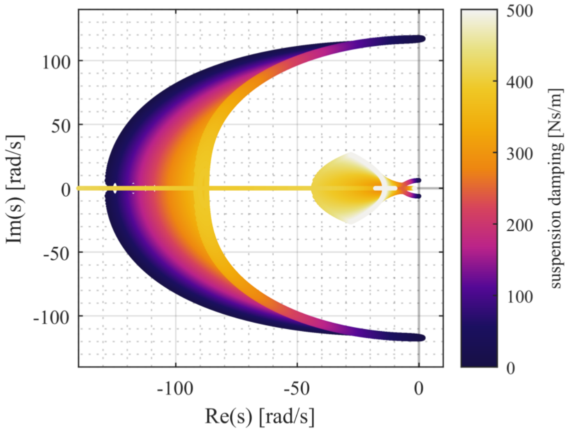

(a) Zoom-in: unsprung mass poles

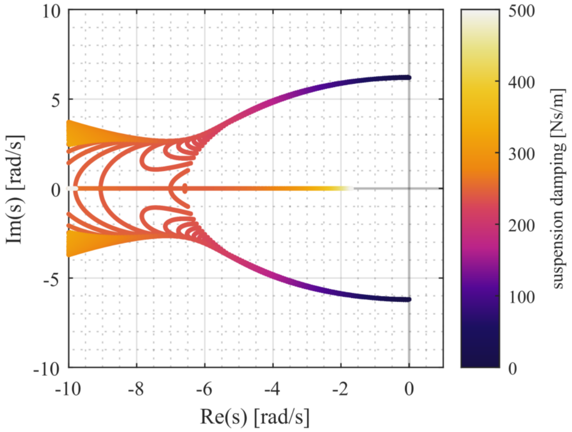

(b) Zoom-in: sprung mass poles

Fig. 9: Root locus of the two-degree-of-freedom system at increasing longitudinal speed and different suspension damping values (color map).

freedom, as these frequencies are more than one decade apart.

To tune the suspension damping, we produce different root loci at increasing $v$ and different values of $c_\mathrm{s}$. This approach allows identifying the damping value that maximizes the horizontal distance between the poles and the imaginary axis. A color map with this parametric sweep is illustrated in Fig. 9. The addition of damping pushes all the mechanical poles to the left side of the complex plane. The poles of the sprung mass, which initially were imaginary, become complex and assume a real part directly proportional to the suspension damping. When $c_\mathrm{s} = 237.4\ \mathrm{Ns/m}$, these poles merge and become real. Additional damping pushes one of these real poles towards the origin, which is unwanted. Thus, $c_\mathrm{s,opt} = 237.4\ \mathrm{Ns/m}$ is the optimal damping value to stabilize the system.

This situation is depicted more clearly in Fig. 10. Inside the whole speed range, we identify the pole that has

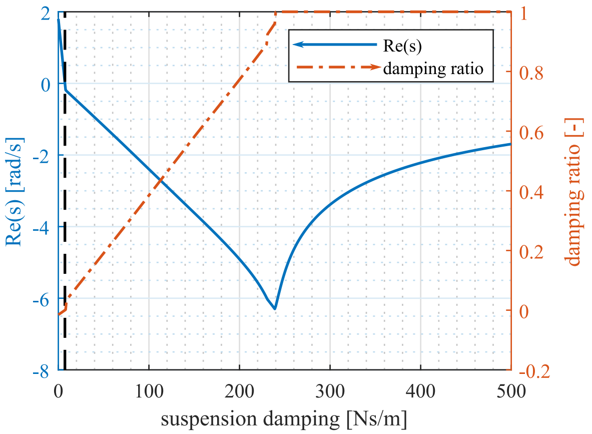

Fig. 10: Suspension damping optimization. Real part of the pole closest to instability in the whole speed range as a function of the suspension damping (left axis, solid). Damping ratio of the pole closest to instability in the whole speed range as a function of the suspension damping (right axis, dash-dot). The cursor indicates the damping threshold between stable and unstable behavior (dashed).

the largest real part and extract this value. The damping ratio $\zeta$ of this pole is also calculated as

$$\zeta = \cos\left(\arctan\frac{\mathrm{Im}(s)}{\mathrm{Re}(s)}\right) \tag{40}$$

This process is repeated for all the tested suspension values. The obtained behavior is piece-wise: the first portion is inherent to the unsprung mass, which is stabilized by a very low damping value $c_\mathrm{s} = 7.25\ \mathrm{Ns/m}$. Below this amount of damping, the system is unstable, as demonstrated by $\mathrm{Re}(s)$ and $\zeta$, which are both negative.

The remainder of the response is convex and belongs to the sprung mass degree of freedom. At low suspension damping, the sprung-mass poles are complex and $\zeta$ is directly proportional to $c_\mathrm{s}$. When the damping ratio reaches $\zeta = 1$, optimal stability is reached, thus confirming $c_{\mathrm{s,opt}} = 237.4\ \mathrm{Ns/m}$. Subsequent results at higher damping yield real poles with $\zeta = 1$, but also a lower degree of stability.

## 4 Numerical Validation

Simulations in the time and the frequency domains were carried out to validate the present approach. In particular, the stability analysis through root loci relies on a linearized version of the two-degree-of-freedom model. Therefore, its verification with the nonlinear representation is needed.

Figure 11 illustrates the natural response of the system in its linear and nonlinear variants to different initial conditions of the pad vertical velocity. This is equivalent to imposing a vertical force impulse disturbance on the pad. The linear model uses the representation described in Appendix B.

The obtained responses present a perfect match in steady-state conditions, as expected. They are both sta-

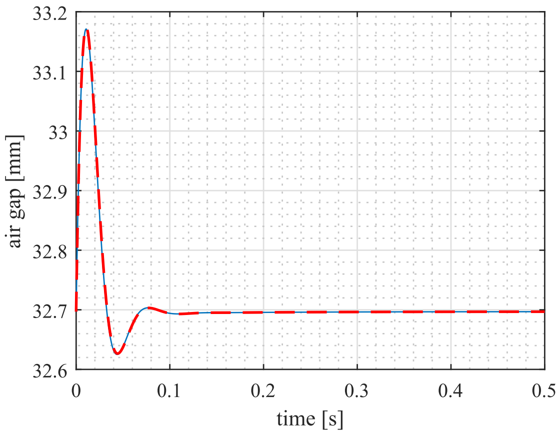

(a) $\dot{z}_{\mathrm{p}}(t=0)=0.1\ \mathrm{m/s}$

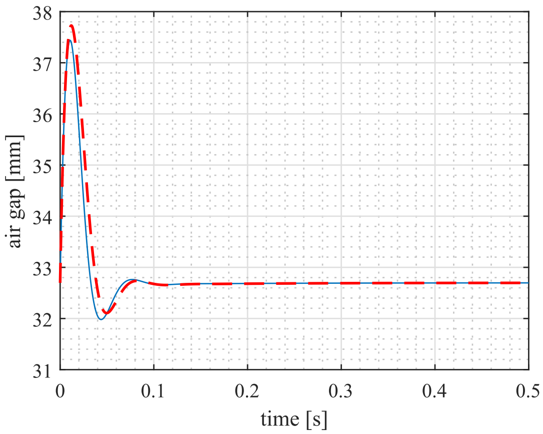

(b) $\dot{z}_{\mathrm{p}}(t=0)=1\ \mathrm{m/s}$

Fig. 11: Natural response of the quarter-car model in its nonlinear (dashed) and linear (solid) variants. The initial vertical velocity of the pad $\dot{z}_{\mathrm{p}}(t=0)$ is set to a non-null value.

ble due to the application of the optimal damping coefficient $c_{\mathrm{s,opt}}$. During transients, differences will appear depending on how far the instantaneous air gap is from the linearization point. When assuming an initial condition $\dot{z}_{\mathrm{p}}(t=0)=1\ \mathrm{m/s}$, the air gap presents a maximum variation of 4.8 mm with respect to its nominal value. Consequently, there is an air gap maximum discrepancy of 0.3 mm among models. In contrast, when reducing the initial condition to $\dot{z}_{\mathrm{p}}(t=0)=0.1\ \mathrm{m/s}$, no relevant discrepancy is observed between the linear and nonlinear representations.

Furthermore, Fig. 12 shows the frequency response functions for

$$H_{\mathrm{a}}(s)=\frac{\ddot{z}_{\mathrm{s}}(s)}{z_{\mathrm{in}}(s)} \tag{41}$$

$$H_{\mathrm{z}}(s)=\frac{z_{\mathrm{p}}(s)}{z_{\mathrm{in}}(s)} \tag{42}$$

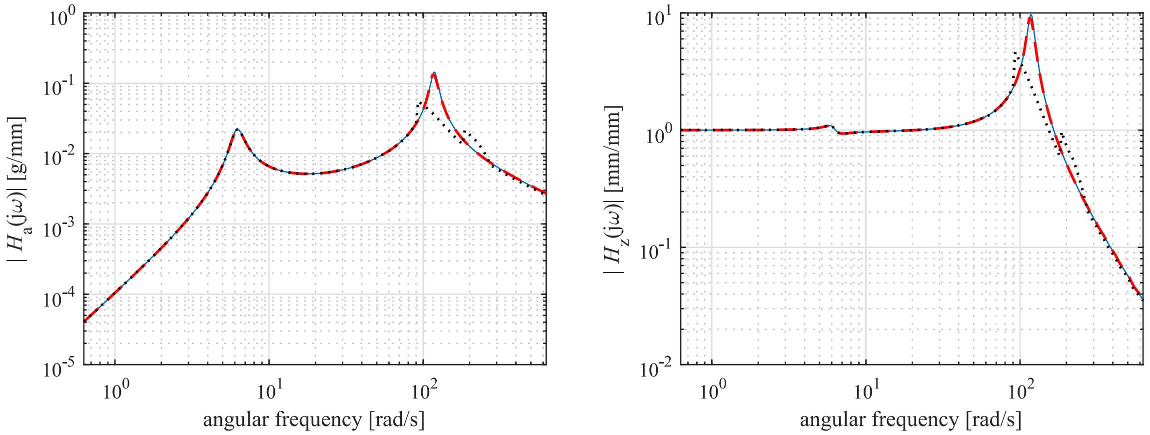

(a) $c_s = c_{s,opt}/10$

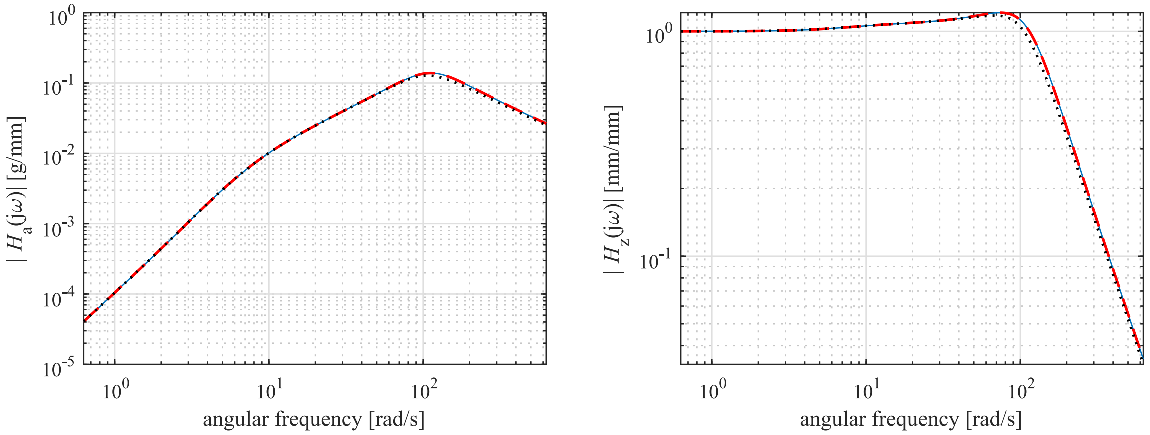

(b) $c_s = c_{s,opt}$

Fig. 12: Magnitude of the frequency response functions for $H_a$ (left) and $H_z$ (right). The linear model response (solid) is compared to the nonlinear response for sinusoidal track profiles of amplitude $0.5\,\mathrm{mm}$ (dashed) and $5\,\mathrm{mm}$ (dotted). Results are presented for two different suspension damping values.

where $z_{in}$ denotes sinusoidal input profile on the surface of the track.

Results in the frequency domain exhibit two mechanical poles at $6.28\,\mathrm{rad/s}$ (sprung mass) and $118.13\,\mathrm{rad/s}$ (pad), respectively. They also confirm what was observed in the time domain. When applying low-amplitude excitation (0.5 mm), both the linear and nonlinear behavior match each other. On the contrary, high-amplitude disturbances (5 mm) will induce discrepancies on the dynamic behavior, especially for what concerns the mechanical pole of the pad. It is worth noting that the application of the optimal damping value is crucial in reducing oscillations and contributing to a close match between linear and nonlinear models.

## 5 Conclusions

The present paper dealt with the stabilization of electrodynamic levitation systems. To this end, a general, multi-domain modeling approach through lumped parameters was proposed and validated using a finite-element model. It was demonstrated that the use of an equivalent circuit with multiple *RL* branches in parallel is useful to capture the conductor current dynamics, especially when dealing with skin effect phenomena.

The obtained electromagnetic model was subsequently coupled to mechanical subsystems and linearized to study stability with root loci. For a single degree of freedom, instability was observed starting at very low speeds. To stabilize the system, damping was introduced by means of a suspension in a two-degree-of-freedom setup. First, the unstable nature of this configuration was identified in the absence of dissipative elements. Then, a parametric variation of the suspension damping was performed to identify the value that optimized the system stability.

Finally, linear and nonlinear representations of the two-degree-of-freedom model were compared in the time and frequency domains. The validity of the linear model was proven due to its favorable match with the nonlinear variant.

Although this paper only explored the stabilization of vertical dynamics for a system with two degrees of freedom, the proposed multi-domain approach can be extended to models with several degrees of freedom.

## References

[1] Marelli, L., Tsakalidis, A., Gkoumas, K., Haq, A., Grosso, M., and Pekar, F., 2017. Strategic transport research and innovation agenda (STRIA) roadmap factsheets.

[2] Burkhard, N., 2014. Why invent the Hyperloop?

[3] SpaceX, 2013. Hyperloop Alpha.

[4] Post, R. F., and Ryutov, D., 1996. The Inductrack concept: A new approach to magnetic levitation. Tech. Rep. UCRL-ID-124115, Lawrence Livermore National Lab., CA (United States), May.

[5] Kusada, S., Igarashi, M., Nemoto, K., Okutomi, T., Hirano, S., Kuwano, K., Tominaga, T., Terai, M., Kuriyama, T., Tasaki, K., Tosaka, T., Marukawa, K., Hanai, S., Yamashita, T., Yanase, Y., Nakao, H., and Yamaji, M., 2007. “The Project Overview of the HTS Magnet for Superconducting Maglev”. *IEEE Transactions on Applied Superconductivity,* **17**(2), June, pp. 2111–2116.

[6] Tonoli, A., 2007. “Dynamic characteristics of eddy current dampers and couplers”. *Journal of Sound and Vibration,* **301**(3-5), Apr., pp. 576–591.

[7] Tonoli, A., Amati, N., Impinna, F., and Detoni, J. G., 2011. “A Solution for the Stabilization of Electrodynamic Bearings: Modeling and Experimental Validation”. *Journal of Vibration and Acoustics,* **133**(2), p. 021004.

[8] Impinna, F., Detoni, J. G., Amati, N., and Tonoli, A., 2013. “Passive Magnetic Levitation of Rotors on Axial Electrodynamic Bearings”. *IEEE Transactions on Magnetics,* **49**(1), Jan., pp. 599–608.

[9] Detoni, J., Impinna, F., Tonoli, A., and Amati, N., 2012. "Unified modelling of passive homopolar and heteropolar electrodynamic bearings". *Journal of Sound and Vibration,* **331**(19), Sept., pp. 4219–4232.

[10] Filatov, A., and Maslen, E., 2001. "Passive magnetic bearing for flywheel energy storage systems". *IEEE Transactions on Magnetics,* **37**(6), Nov., pp. 3913–3924.

[11] Lembke, T. A., 2005. "Design and analysis of a novel low loss homopolar electrodynamic bearing". PhD thesis, School of Electrical Engineering, KTH, Stockholm, Sweden.

[12] Lembke, T. A., 2014. "Review of Electrodynamic Bearings". In ISMB14, 14th International Symposium on Magnetic Bearings.

[13] Lembke, T. A., 2008. Electrodynamic Actuator. patent application WO2010064978.

[14] Lembke, T. A., 2012. "1-DOF Bearing Arrangement with Passive Radial Bearings and Highly Efficient Integrated Electrodynamic Dampers, EDD". In Proceedings of ISMB13, pp. 1–7.

[15] Van Verdeghem, J., Kluyskens, V., and Dehez, B., 2017. "Five degrees of freedom linear state-space representation of electrodynamic thrust bearings". *Journal of Sound and Vibration,* **405**, Sept., pp. 48–67.

[16] Van Verdeghem, J., Kluyskens, V., and Dehez, B., 2019. "Stability and Performance Analysis of Electrodynamic Thrust Bearings". *Actuators,* **8**(1), Mar., p. 11.

[17] Post, R., and Ryutov, D., 2000. "The Inductrack: a simpler approach to magnetic levitation". *IEEE Transactions on Appiled Superconductivity,* **10**(1), pp. 901–904.

[18] Post, R. F., 1998. Inductrack demonstration model. Tech. Rep. UCRL-ID-129664, Lawrence Livermore National Lab., CA (United States), Feb.

[19] Gurol, S., and Baldi, B., 2004. "Overview of the General Atomics Urban Maglev Technology Development Program". In Proceedings of the 2004 IEEE/ASME Joint Rail Conference, pp. 187–191.

[20] Gurol, H., Baldi, R., Jeter, P., Kim, I.-K., Bever, D., and Atomics, G., 2005. General atomics low speed maglev technology development program (Supplemental# 3). Tech. rep., United States. Federal Transit Administration. Office of Technology.

[21] Storset, O., and Paden, B., 2002. "Infinite dimensional models for perforated track electrodynamic magnetic levitation". In Proceedings of the 41st IEEE Conference on Decision and Control, 2002., Vol. 1, IEEE, pp. 842–847.

[22] Tsunashima, H., and Abe, M., 1998. "Static and dynamic performance of permanent magnet suspension for maglev transport vehicle". *Vehicle System Dynamics,* **29**(2), pp. 83–111.

[23] Pradhan, R., and Katyayan, A., 2018. "Vehicle dynamics of permanent-magnet levitation based Hyperloop capsules". In ASME 2018 Dynamic Systems and Control Conference, p. V002T22A004.

[24] Íñiguez, J., and Raposo, V., 2009. "Laboratory scale prototype of a low-speed electrodynamic levitation

system based on a Halbach magnet array". *European Journal of Physics,* **30**(2), Mar., pp. 367–379.

[25] Indraneel, T., Jayakumar, V., Soni, A., Shiyani, D. R., Tyagi, K., and Abdallah, S., 2019. "Levitation array testing for Hyperloop pod design". In AIAA Scitech 2019 Forum, p. 0787.

[26] Duan, J., Xiao, S., Zhang, K., Rotaru, M., and Sykulski, J. K., 2019. "Analysis and optimization of asymmetrical double-sided electrodynamic suspension devices". *IEEE Transactions on Magnetics,* **55**(6), pp. 1–5.

[27] Khan, M. M., 2019. "Development of Ryerson's First Hyperloop Pod for systems using a modular approach". In ICASSE 2019, The International Conference on Aerospace System Science and Engineering, p. 90.

[28] Opgenoord, M. M. J., Merian, C., Mayo, J., Kirschen, P., O'Rourke, C., Izatt, G., et al., 2017. MIT Hyperloop final report. Tech. rep., Massachusetts Institute of Technology, Cambridge, Massachusetts.

[29] SpaceX, 2016. SpaceX Hyperloop test-track specification.

[30] Pyrhonen, J., Jokinen, T., and Hrabovcová, V., 2008. *Design of rotating electrical machines*. Wiley, Chichester, West Sussex, UK.

[31] Bianchi, N., 2005. *Electrical machine analysis using finite elements*. CRC press, Boca Raton, FL, USA.

## Appendix A: General State-Space Representations for Stability Analysis

### Single degree of freedom

$$\mathbf{x}_1 = \left\{ i_{\mathrm{d},1}\ i_{\mathrm{q},1}\ i_{\mathrm{d},2}\ i_{\mathrm{q},2} \cdots i_{\mathrm{d},N_\mathrm{b}}\ i_{\mathrm{q},N_\mathrm{b}}\ \dot{z}_\mathrm{p}\ z_\mathrm{p} \right\}^\mathsf{T} \tag{43}$$

$$\mathbf{A}_1 = \begin{bmatrix} -\omega_{\mathrm{p},1} & \omega & 0 & 0 & \cdots & 0 & 0 & \frac{\Lambda_0}{\gamma L_1}\mathrm{e}^{-\frac{z_{\mathrm{p},0}}{\gamma}} & 0 \\ -\omega & -\omega_{\mathrm{p},1} & 0 & 0 & \cdots & 0 & 0 & 0 & \frac{\omega\Lambda_0}{\gamma L_1}\mathrm{e}^{-\frac{z_{\mathrm{p},0}}{\gamma}} \\ 0 & 0 & -\omega_{\mathrm{p},2} & \omega & \cdots & 0 & 0 & \frac{\Lambda_0}{\gamma L_2}\mathrm{e}^{-\frac{z_{\mathrm{p},0}}{\gamma}} & 0 \\ 0 & 0 & -\omega & -\omega_{\mathrm{p},2} & \cdots & 0 & 0 & 0 & \frac{\omega\Lambda_0}{\gamma L_2}\mathrm{e}^{-\frac{z_{\mathrm{p},0}}{\gamma}} \\ \vdots & \vdots & \vdots & \vdots & \ddots & \vdots & \vdots & \vdots & \vdots \\ 0 & 0 & 0 & 0 & \cdots & -\omega_{\mathrm{p},N_\mathrm{b}} & \omega & \frac{\Lambda_0}{\gamma L_{N_\mathrm{b}}}\mathrm{e}^{-\frac{z_{\mathrm{p},0}}{\gamma}} & 0 \\ 0 & 0 & 0 & 0 & \cdots & -\omega & -\omega_{\mathrm{p},N_\mathrm{b}} & 0 & \frac{\omega\Lambda_0}{\gamma L_{N_\mathrm{b}}}\mathrm{e}^{-\frac{z_{\mathrm{p},0}}{\gamma}} \\ -\frac{2\Lambda_0}{\gamma m_\mathrm{t}}\mathrm{e}^{-\frac{z_{\mathrm{p},0}}{\gamma}} & 0 & -\frac{2\Lambda_0}{\gamma m_\mathrm{t}}\mathrm{e}^{-\frac{z_{\mathrm{p},0}}{\gamma}} & 0 & \cdots & -\frac{2\Lambda_0}{\gamma m_\mathrm{t}}\mathrm{e}^{-\frac{z_{\mathrm{p},0}}{\gamma}} & 0 & 0 & 0 \\ 0 & 0 & 0 & 0 & \cdots & 0 & 0 & 1 & 0 \end{bmatrix} \tag{44}$$

### Two degrees of freedom

$$\mathbf{x}_2 = \left\{ i_{\mathrm{d},1}\ i_{\mathrm{q},1}\ i_{\mathrm{d},2}\ i_{\mathrm{q},2} \cdots i_{\mathrm{d},N_\mathrm{b}}\ i_{\mathrm{q},N_\mathrm{b}}\ \dot{z}_\mathrm{p}\ z_\mathrm{p}\ \dot{z}_\mathrm{s}\ z_\mathrm{s} \right\}^\mathsf{T} \tag{45}$$

$$\mathbf{A}_2 = \begin{bmatrix} -\omega_{\mathrm{p},1} & \omega & 0 & 0 & \cdots & 0 & 0 & \frac{\Lambda_0}{\gamma L_1}\mathrm{e}^{-\frac{z_{\mathrm{p},0}}{\gamma}} & 0 & 0 & 0 \\ -\omega & -\omega_{\mathrm{p},1} & 0 & 0 & \cdots & 0 & 0 & 0 & \frac{\omega\Lambda_0}{\gamma L_1}\mathrm{e}^{-\frac{z_{\mathrm{p},0}}{\gamma}} & 0 & 0 \\ 0 & 0 & -\omega_{\mathrm{p},2} & \omega & \cdots & 0 & 0 & \frac{\Lambda_0}{\gamma L_2}\mathrm{e}^{-\frac{z_{\mathrm{p},0}}{\gamma}} & 0 & 0 & 0 \\ 0 & 0 & -\omega & -\omega_{\mathrm{p},2} & \cdots & 0 & 0 & 0 & \frac{\omega\Lambda_0}{\gamma L_2}\mathrm{e}^{-\frac{z_{\mathrm{p},0}}{\gamma}} & 0 & 0 \\ \vdots & \vdots & \vdots & \vdots & \ddots & \vdots & \vdots & \vdots & \vdots & \vdots & \vdots \\ 0 & 0 & 0 & 0 & \cdots & -\omega_{\mathrm{p},N_\mathrm{b}} & \omega & \frac{\Lambda_0}{\gamma L_{N_\mathrm{b}}}\mathrm{e}^{-\frac{z_{\mathrm{p},0}}{\gamma}} & 0 & 0 & 0 \\ 0 & 0 & 0 & 0 & \cdots & -\omega & -\omega_{\mathrm{p},N_\mathrm{b}} & 0 & \frac{\omega\Lambda_0}{\gamma L_{N_\mathrm{b}}}\mathrm{e}^{-\frac{z_{\mathrm{p},0}}{\gamma}} & 0 & 0 \\ -\frac{2\Lambda_0}{\gamma m_\mathrm{p}}\mathrm{e}^{-\frac{z_{\mathrm{p},0}}{\gamma}} & 0 & -\frac{2\Lambda_0}{\gamma m_\mathrm{p}}\mathrm{e}^{-\frac{z_{\mathrm{p},0}}{\gamma}} & 0 & \cdots & -\frac{2\Lambda_0}{\gamma m_\mathrm{p}}\mathrm{e}^{-\frac{z_{\mathrm{p},0}}{\gamma}} & 0 & -\frac{c_\mathrm{s}}{m_\mathrm{p}} & -\frac{k_\mathrm{s}}{m_\mathrm{p}} & \frac{c_\mathrm{s}}{m_\mathrm{p}} & \frac{k_\mathrm{s}}{m_\mathrm{p}} \\ 0 & 0 & 0 & 0 & \cdots & 0 & 0 & 1 & 0 & 0 & 0 \\ 0 & 0 & 0 & 0 & \cdots & 0 & 0 & \frac{c_\mathrm{s}}{m_\mathrm{s}} & \frac{k_\mathrm{s}}{m_\mathrm{s}} & -\frac{c_\mathrm{s}}{m_\mathrm{s}} & -\frac{k_\mathrm{s}}{m_\mathrm{s}} \\ 0 & 0 & 0 & 0 & \cdots & 0 & 0 & 0 & 0 & 1 & 0 \end{bmatrix} \tag{46}$$

## Appendix B: Two-Degree-of-Freedom Linear Model for Numerical Validation

$$\dot{\mathbf{x}}_3 = \mathbf{A}_3\mathbf{x}_3 + \mathbf{B}\mathbf{u} \tag{47}$$

$$\mathbf{y} = \mathbf{C}\mathbf{x}_3 + \mathbf{D}\mathbf{u} \tag{48}$$

$$\mathbf{x}_3 = \begin{Bmatrix} \mathbf{x}_2 \; z_{\mathrm{in}} \end{Bmatrix}^{\mathsf{T}} \tag{49}$$

$$\mathbf{A}_3 = \begin{bmatrix} \mathbf{A}_2 & \mathbf{a} \\ \mathbf{0} & 0 \end{bmatrix} \tag{50}$$

$$\mathbf{a} = \begin{bmatrix} 0 \; -\frac{\omega\Lambda_0}{\gamma L_1}\mathrm{e}^{-\frac{z_{\mathrm{p},0}}{\gamma}} \; 0 \; -\frac{\omega\Lambda_0}{\gamma L_2}\mathrm{e}^{-\frac{z_{\mathrm{p},0}}{\gamma}} \; \cdots \; 0 \; -\frac{\omega\Lambda_0}{\gamma L_{N_{\mathrm{b}}}}\mathrm{e}^{-\frac{z_{\mathrm{p},0}}{\gamma}} \; 0 \; 0 \; 0 \; 0 \end{bmatrix}^{\mathsf{T}} \tag{51}$$

$$\mathbf{u} = \dot{z}_{\mathrm{in}} \tag{52}$$

$$\mathbf{B} = \begin{bmatrix} -\frac{\Lambda_0}{\gamma L_1}\mathrm{e}^{-\frac{z_{\mathrm{p},0}}{\gamma}} \; 0 \; -\frac{\Lambda_0}{\gamma L_2}\mathrm{e}^{-\frac{z_{\mathrm{p},0}}{\gamma}} \; 0 \cdots \; -\frac{\Lambda_0}{\gamma L_{N_{\mathrm{b}}}}\mathrm{e}^{-\frac{z_{\mathrm{p},0}}{\gamma}} \; 0 \; 0 \; 0 \; 0 \; 0 \; 1 \end{bmatrix}^{\mathsf{T}} \tag{53}$$

$$\mathbf{y} = \begin{Bmatrix} z_{\mathrm{p}} \; \dot{z}_{\mathrm{s}} \end{Bmatrix}^{\mathsf{T}} \tag{54}$$

$$\mathbf{C} = \begin{bmatrix} 0\;0\;0\;0 \cdots 0\;0\;0\;1\;0\;0\;0 \\ 0\;0\;0\;0 \cdots 0\;0\;0\;0\;1\;0\;0 \end{bmatrix} \tag{55}$$

$$\mathbf{D} = \begin{bmatrix} 0\;0 \end{bmatrix}^{\mathsf{T}} \tag{56}$$

## List of Figures

## List of Tables